Compact and Foldable Hip Exoskeleton With High Torque Density Actuator for Walking and Stair-Climbing Assistance in Young and Older Adults

Yuming Yan, Jin Sen Huang, Junxi Zhu, *Graduate Student Member, IEEE*, Zhimin Hou, Weibo Gao, *Graduate Student Member, IEEE*, Ivan Lopez-Sanchez, Nitin Srinivasan, Advaith Srihari, and Hao Su, *Senior Member, IEEE*

***Abstract*—Exoskeletons hold great potential to enhance human locomotion performance, but their development is often hindered by bulky, heavy, and obtrusive actuator and mechanism designs. Here, we present a compact and lightweight hip exoskeleton endowed with a custom high torque density actuator and two foldable mechanisms, namely foldable waist belt with self-alignment mechanism and foldable thigh brace with self-adjusting linear slider mechanism. Our model of actuator electromagnetic design considered four design parameters, including end winding length, stator teeth number, rotor pole pair number, and gear ratio that are tailored for portable exoskeletons. Two foldable mechanism enhanced exoskeleton adaptability and user comfort. Benchtop experimental results demonstrated that our actuator can provide an 18 N · m peak torque with a packaging factor improvement of 27% in contrast with state-of-the-art actuators used in exoskeletons. The volume of our exoskeleton was reduced by 55% and the weight was reduced from 3.7 to 2.7 kg compared to our prior design. Preliminary human experiments demonstrated the feasibility of our exoskeleton to reduce metabolic rate during walking and stair climbing for young and older adults.**

***Index Terms*—High torque density actuators, hip exoskeletons, older, wearable robots.**

I. Introduction

EXOSKELETONS have demonstrated potential in assisting human movement, such as improving walking for individuals with disabilities [1], [2], [3]. More recently, they have also been shown to enhance walking efficiency for non-disabled individuals [4], [5], [6]. However, the widespread adoption remains limited due to their bulkiness and weight, which restrict usability for a broader range of users. To address these limitations, our vision is to transform exoskeletons into consumer-grade devices that seamlessly support daily activities for personal mobility assistance. To achieve this goal, exoskeletons must satisfy several critical criteria, e.g., be compact, lightweight, and unobtrusive, ensuring they do not interfere with common daily activities, such as sitting inside a car or in a chair. In addition, they should be designed to be worn discreetly under clothing, preserving users' dignity and promoting greater social acceptance.

The first challenge in exoskeleton mechatronics design stems from the limitations of actuators, which struggle to achieve high torque density in a compact form factor. Most state-of-the-art exoskeletons rely on commercially available conventional actuators (e.g., standard Maxon motors) that are primarily optimized for high-speed applications rather than the low-speed, high-torque requirements of human assistance. To address this challenge, recent studies explored quasi-direct-drive actuators [15] for exoskeletons but have provided limited modeling and theoretical analysis of actuator design. Specifically, these studies focused on optimizing gear ratios and motor air gaps but

Received 26 January 2025; revised 16 April 2025; accepted 20 May 2025. Recommended by Technical Editor E. Wu and Senior Editor Z. Sun. This work was supported in part by the National Science Foundation CAREER award CMMI under Grant 1944655, in part by the National Science Foundation Cyber-Physical Systems under Grant 2344956, in part by the National Science Foundation Future of Work under Grant 2231419, in part by the Switzer Research Distinguished Fellow under Grant SFGE22000372, in part by the National Institutes of Health under Grant 1R01EB035404, and in part by the NIH National Institute on Aging under Grant P30AG073104. *(Yuming Yan and Jin Sen Huang contributed equally to this work.) (Corresponding author: Hao Su.)*

This work involved human subjects or animals in its research. Approval of all ethical and experimental procedures and protocols was granted by NCSU Institutional Review Board under Application No. 26017, and performed in line with the Use of Human Subject in Research.

Yuming Yan, Junxi Zhu, Zhimin Hou, Ivan Lopez-Sanchez, and Nitin Srinivasan are with the Lab of Biomechatronics and Intelligent Robotics, Tandon School of Engineering, New York University, New York, NY 11201 USA.

Jin Sen Huang, Weibo Gao, and Advaith Srihari are with the Lab of Biomechatronics and Intelligent Robotics, Tandon School of Engineering, New York University, New York, NY 11201 USA, and also with the North Carolina State University, Raleigh, NC 27606 USA.

Hao Su is with the Lab of Biomechatronics and Intelligent Robotics, Tandon School of Engineering, New York University, New York, NY 11201 USA, also with the Joint NCSU/UNC Department of Biomedical Engineering, North Carolina State University, Raleigh, NC 27606 USA, and also with the University of North Carolina at Chapel Hill, Chapel Hill, NC 27599 USA (e-mail: hao.su@nyu.edu).

This article has supplementary material provided by the authors and color versions of one or more figures available at https://doi.org/10.1109/TMECH.2025.3576123.

Digital Object Identifier 10.1109/TMECH.2025.3576123

TABLE I
BENCHMARK WITH STATE-OF-THE-ART HIP EXOSKELETONS: COMPACT AND FOLDABLE HIP EXOSKELETON WITH HIGH TORQUE DENSITY ACTUATOR

	Exoskeleton mass (kg)	Exoskeleton torque density (Nm/kg)	Exoskeleton width (mm)	Exoskeleton size width × height × thickness (mm)	Gear ratio	Actuator size (mm)	Actuator mass (kg)	Actuator peak torque (Nm)	Actuator torque density (Nm/kg)
Samsung [7]	2.6	4.62	NA	NA	50:1	$\phi 42.8 \times 29.9$	NA	12	NA
Harvard [8]	5.0	6.4	533	$533 \times 440 \times 480$	51:1	$\phi 30 \times 67.3$	1.337	32	23.9
Honda [9]	2.8	2.14	NA	505×311	NA	NA	NA	6	NA
Panasonic [10]	9.3	1.08	610	$610 \times 912 \times 500$	16:1	$\phi 22 \times 99.05$	0.58	10	17.2
SSSA [11]	4.2	2.38	590	$590 \times 586 \times 360$	80:1	68x128x66.8	1.2	10	8.3
ASU [12]	2.95	3.05	478	$478 \times 861 \times 432$	NA	NA	1.135	9	7.9
Gatech [13]	7	2.01	521	$521 \times 788 \times 608$	NA	$\phi 30 \times 99$	1.5	14.1	9.4
Our prior work [14]	3.8	4.74	525	$525 \times 350 \times 220$	9:1	$\phi 98 \times 38.5$	0.49	18	36.7
This work	**2.7**	**6.67** (highest)	**460**	$\mathbf{460 \times 180 \times 220}$	**9.67:1**	$\boldsymbol{\phi 80 \times 37}$	**0.38**	**18**	**47.4** (highest)

The bold values highlight the specifications of our hip exoskeleton.

overlooked critical aspects, such as the design of stator end winding lengths and the configuration of the motor's stator teeth and rotor pole pairs. Off-the-shelf motors often feature distributed windings with long end turns, which increase thickness and reduce torque density [16]. Furthermore, the arrangement of stator teeth and rotor pole pairs is crucial for sufficient output torque. The lack of an electromagnetic model of actuator design has created a bottleneck, hindering the development of compact, lightweight, and unobtrusive portable exoskeletons capable of addressing the multifaceted needs of daily living activities [17].

The second challenge of exoskeleton mechatronic design lies in achieving a balance between structural integrity, user comfort, and practical usage. State-of-the-art exoskeletons typically employ rigid frames on the waist or thigh to ensure effective assistance transmission at the cost of increased hindrance in daily activities [18]. Moreover, the rigid frame designs often fail to adequately adapt to the users' body contours, leading to discomfort during prolonged wear and compromised force transmission between the device and the user [19], [20]. Furthermore, this mismatch between human anthropometry and robot design geometry can result in misalignment during movement [15], [21], further exacerbates these issues, diminishing both comfort and the effectiveness of assistance.

To address the first challenge of designing compact actuators with high torque density for exoskeletons, our first method is to develop an electromagnetic model to consider the actuator design of high torque density motor with low gear ratio reducer for exoskeletons. First, we derived a motor electromagnetic model to determine motor design parameters to achieve sufficient peak torque within a small size. Then, we designed a fractional slot concentrated winding arrangement, which reduces the end-winding length, improving torque density and maintaining lightness. Finally, we designed stator and rotor pole pairs, a critical factor for achieving sufficient peak torque. Through the motor electromagnetic design, we developed our custom compact quasi-direct-drive actuator with high torque density for a portable powered hip exoskeleton with the design of a planetary reducer with a gear ratio of 9.67:1 (see Table I).

To address the second challenge of compact mechanical structure, we introduced two foldable mechanism designs that enhance user comfort and adaptability without compromising assistance delivery. First, we introduced a foldable waist belt with a self-aligning mechanism that ensures comfort and facilitated portability that was partly inspired by a lower limb exoskeleton [22]. Second, a foldable thigh brace with a self-adjusting mechanism was proposed to accommodate body shape variations and ensure proper alignment during movement while being tolerant to minor misalignment between the actuator and hip joint. The contributions of this work are: 1) we developed an electromagnetic model to consider four key design parameters (stator teeth number, rotor pole pair, end winding length, and gear ratio) of the high torque density motor with a low ratio gear for exoskeletons; 2) we proposed foldable waist belt structure with self-alignment mechanism and foldable thigh brace with self-adjusting linear slider mechanism that enhances exoskeleton adaptability and user comfort without compromising assistance delivery.

II. DESIGN REQUIREMENTS OF COMPACT AND HIGH-TORQUE DENSITY HIP EXOSKELETON

Hip exoskeletons should meet multifaceted requirements for assisting the hip joint. They should be compact and not interfere with the environment even when the robot is not providing physical assistance, such as sitting in a chair or inside a car. Furthermore, the robot should not interfere with adduction/abduction movements. They should assist in daily activities such as walking and stair climbing. Finally, they should fit different sizes of subjects. An overview of our compact and high-torque density hip exoskeleton is shown in Fig. 1.

The peak assistive torque in hip exoskeletons is a critical design factor: higher assistive torque tends to result in metabolic reductions in ideal scenarios, but larger, heavier actuators and exoskeleton structure may hinder their performance. A low peak torque of 6 N · m only led to a minor metabolic rate reduction of 7% in [9], but excessive peak torque will result in an increased metabolic rate due to the extra mass of the robot [23]. Finding a balance between the peak torque and mechanical design (total weight, mass placement, etc.) is a crucial design challenge. Our exoskeleton design is intended to deliver small to medium assistance, specifically within 20% to 30% assistance. Based on biomechanical requirements, the exoskeleton is designed to provide an assistive peak torque of 18 N · m. The hip exoskeleton must satisfy the kinematic and kinetic requirements of the human hip joint. During walking, the hip joint exhibits two degrees of freedom (DOFs): flexion/extension in the sagittal plane and abduction/adduction in the frontal plane. Therefore, the exoskeleton must accommodate both DOFs. For level-ground

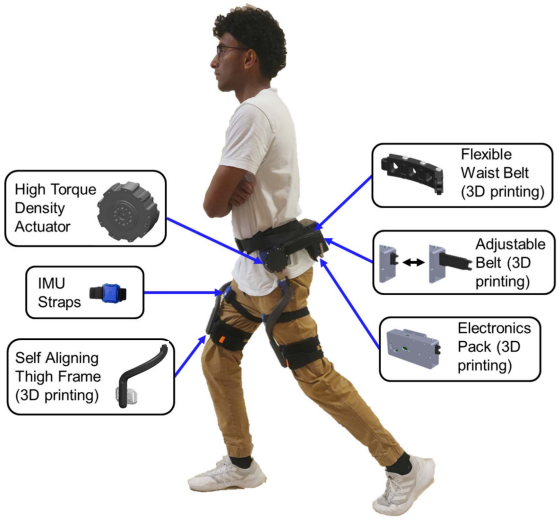

Fig. 1. Our hip exoskeleton (bilateral mass 2.7 kg, 18 N · m peak torque) consists of custom high torque density actuators (method 1), foldable waist belt, and foldable thigh brace (method 2).

TABLE II
DESIGN REQUIREMENTS OF HIP EXOSKELETONS

Parameters	Walking	Stair climbing	Desired	Our prior work	This work
Hip flexion/extension (°)	32.2/22.5	41.9/7.7	60/5	135/60	135/60
Hip abduction/adduction (°)	7.9/6.4	7.9/6.4	7.9/6.4	90/60	90/60
Hip joint peak torque (Nm)	52	59	15	18	18
Hip joint speed (rad/s)	2.3	2.3	5	40.8	32.4
Actuator peak torque density (Nm/kg)	-	-	30	37	47.4
Actuator backdrive torque (Nm)	-	-	0.5	0.51	0.3
Actuator size (mm)	-	-	$\phi 90 \times 40$	$\phi 98 \times 37$	$\phi 80 \times 37$
Exoskeleton weight (kg)	-	-	5	3.8	2.7
Exoskeleton width (mm)	-	-	500	525	460

walking, the typical range of motion (ROM) of the human hip is approximately 32.2° in flexion, 22.5° in extension, 7.9° in abduction, and 6.4° in adduction [15]. To support a wider range of activities and a more diverse user population, our exoskeleton is designed with an extended ROM: 130° flexion, 40° extension, 90° abduction, and 60° adduction, encompassing the maximum limits of the human hip joint. The design requirements are summarized in Table II.

III. ELECTROMAGNETIC DESIGN OF HIGH TORQUE DENSITY MOTORS AND LOW RATIO GEAR

Although brushless direct current (BLDC) motors are popular for exoskeletons, there is limited work on the principle of electric motor design for compact portable exoskeletons. Thus, this section aims to present the design principles of high torque density actuators for exoskeletons. The constraints (see Fig. 2) are determined by the gait kinetics requirements where the actuator is demanded to provide the required torque τ_{req}, torque density $\rho_{\tau\text{req}}$, angular velocity ω_{req} and backdrive torque $\tau_{b\text{req}}$. Based on the human–robot interaction model, the actuator output includes $\tau_{\max(l_{\text{end}},p_s,p_r,n)}$, $\rho_{\tau\max(l_{\text{end}},p_s,p_r,n)}$, $\omega_{\max(l_{\text{end}},p_s,p_r,n)}$, and $\tau_{\text{bpeak}(l_{\text{end}},p_s,p_r,n)}$. With the input of four design parameters $(l_{\text{end}}, p_s, p_r, n)$ and human–robot interaction principle, the output $(\tau_{\max}, \rho_{\tau\max}, \omega_{\max}$, and $\tau_{\text{bpeak}})$ can be formulated to fulfill the constraints of hip exoskeletons (τ_{req}, $\rho_{\tau\text{req}}$, ω_{req}, and $\tau_{b\text{req}}$). The design parameters and performance of our actuator are listed in Tables IV and V.

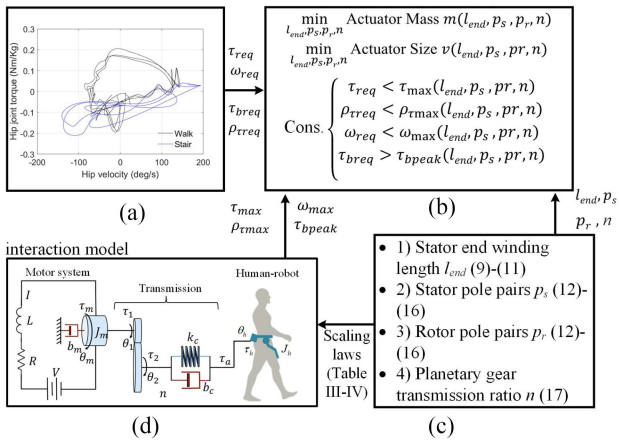

Fig. 2. Principle of BLDC actuator with four design parameters. (a) Constraints are produced by gait kinetics including required peak torque τ_{req}, angular velocity ω_{req}, backdrive torque $\tau_{b\text{req}}$, and torque density $\rho_{t\text{req}}$. (b) Model of actuator electromagnetic design, considering actuator mass, size, and motor capability in terms of $\tau_{\max(l_{\text{end}},p_s,p_r,n)}$, $\rho_{t\max(l_{end},p_s,p_r,n)}$, $\omega_{\max(l_{\text{end}},p_s,p_r,n)}$, and $\tau_{b\text{peak}(l_{\text{end}},p_s,p_r,n)}$ to meet design requirements. (c) Four design parameters of our actuator for exoskeleton: end winding length, stator teeth number, rotor pole pairs, and gear ratio. (d) Human–robot interaction model to denote required actuator performance.

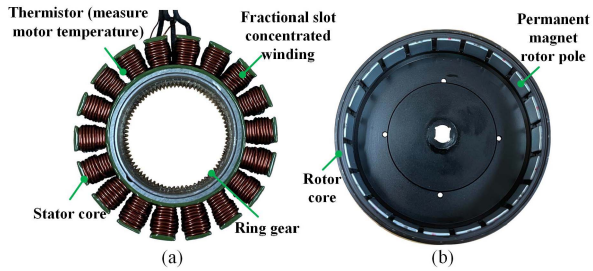

Fig. 3. Our custom motor with high torque density. (a) Stator assembly with 18 stator teeth (see Fig. 6 for details). (b) Frameless exterior rotor assembly with 10 pole pairs.

A. Model of Actuator Electromagnetic Design

Figs. 3 and 4 illustrate our BLDC motor featuring a double-layer, nonoverlapping concentrated winding configuration. Each stator tooth consists of a salient iron tooth encased by a nonoverlapping concentrated armature coil. The rotor employs surface-mounted, radially magnetized, tile-shaped permanent magnets. The relationships between key design parameters and output torque performance are derived from motor power and sizing equations. Assuming a sinusoidal flux linkage and neglecting winding resistance, the input power of the m-phase motor can be expressed as [24]

$$P_{\text{in}} = \frac{m}{T}\int_0^T E_m \sin(\omega_e t)\, I_m \sin(\omega_e t)\, dt = \frac{m}{2} E_m I_m \quad (1)$$

where m is the number of phases, E_m denotes the peak value of the back electromotive force, I_m is the peak value of the phase current, T corresponds to the sine wave period, and ω_e is the electrical rotating speed. The permanent magnet flux per coil

TABLE III
STATOR TEETH AND ROTOR POLE COMBINATIONS DETERMINATION

Pole / Teeth	Eq.	4	6	8	10	12	14	16	20	22	24	26	28	30
9	SPP (18) k_w (13)-(16) T_{cog} (17)	3/4 0.617 36	1/2 0.866 18	3/8 0.945 72	3/10 0.945 90	1/4 0.866 36	3/14 0.617 126	3/16 0.328 144	3/20 0.328 180	3/22 0.617 198	1/8 0.866 72	3/26 0.945 234	3/28 0.945 252	1/10 0.866 90
12	SPP (18) k_w (13)-(16) T_{cog} (17)	1/1 0.500 12	2/3 0.707 12	1/2 0.866 24	2/5 0.933 60	-	2/7 0.933 84	1/4 0.866 48	1/5 0.500 60	2/11 0.250 132	-	2/13 0.250 156	1/7 0.500 84	2/15 0.500 60
15	SPP (18) k_w (13)-(16) T_{cog} (17)	5/4 0.389 60	5/6 0.543 30	5/8 0.711 120	1/2 0.866 30	5/12 0.878 60	5/14 0.951 210	5/16 0.951 240	1/4 0.866 60	5/22 0.711 330	5/24 0.543 120	5/26 0.389 390	5/28 0.199 420	-
18	SPP (18) k_w (13)-(16) T_{cog} (17)	3/2 0.328 36	1/1 0.500 18	3/4 0.617 72	3/5 0.735 90	1/2 0.866 36	3/7 0.902 126	3/8 0.945 144	3/10 0.945 180	3/11 0.902 198	1/4 0.866 72	3/13 0.735 234	3/14 0.617 126	1/5 0.500 90
21	SPP (18) k_w (13)-(16) T_{cog} (17)	7/4 0.282 84	7/6 0.399 42	7/8 0.538 168	7/10 0.650 210	7/12 0.720 84	1/2 0.866 42	7/16 0.890 336	7/20 0.953 420	7/22 0.953 462	7/24 0.897 168	7/26 0.890 546	1/4 0.866 84	7/30 0.720 210
24	SPP (18) k_w (13)-(16) T_{cog} (17)	2/1 0.250 24	4/3 0.361 24	1/1 0.500 24	4/5 0.583 120	2/3 0.707 24	4/7 0.760 168	1/2 0.866 48	2/5 0.933 120	4/11 0.949 264	-	4/13 0.949 312	2/7 0.933 168	4/15 0.805 120

TABLE IV
FINAL DESIGN PARAMETERS OF OUR FRACTIONAL SLOT CONCENTRATED WINDING MOTOR AND GEAR RATIO

Symbol	Design variable	Value	Unit
l_{end}	Stator end winding length	1.7	mm
Q	Number of stator teeth	18	-
p_r	Number of rotor pole pairs	10	-
n	Gear ratio	9.67:1	-

TABLE V
CHARACTERISTICS OF OUR HIGH TORQUE DENSITY ACTUATOR AND BENCHMARK WITH STATE-OF-THE-ART ACTUATORS

Parameters	Maxon EC45	MyActuator RMD-X8	Our prior work [14] T-motor AK80-9	This work Our actuator
Line resistance (Ω)	0.608	0.53	0.34	0.224
Line inductance (mH)	0.46	0.21	0.114	0.235
Peak torque (Nm)	1.46	18	18	18
Weight (g)	**141**	**660**	**485**	**380**
Size (mm)	$\phi 43 \times 30$	$\phi 98 \times 45.5$	$\phi 98 \times 38.5$	$\phi 80 \times 37$
Volume (L)	43.5	343.0	290.3	185.9
Package factor (mNm/L)	**33.6**	**52.5**	**62.0**	**96.8**
Torque density (Nm/kg)	**10.4**	**27.3**	**37.1**	**47.4**
Nominal speed (rpm)	4860	190	245	310
Back drive torque (Nm)	-	-	-	0.3
Nominal current (A)	3.21	3.5	12	10
Nominal voltage (V)	24	48	24	24

The bold values highlight key specifications when used in exoskeleton applications.

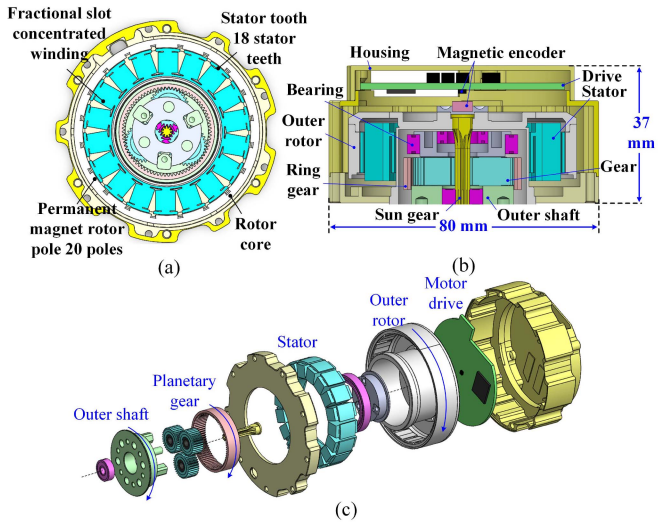

Fig. 4. (a) Our highly integrated actuator, including a BLDC motor with 18-stator-teeth, 10-rotor-pole-pairs, a double-layer nonoverlapping fractional slot concentrated winding, and a 9.67:1 low gear ratio. (b) Cross-sectional view of the mechatronic design of our compact actuator composed of motor, gear, and motor driver with embedded sensors. (c) Outer rotor of our motor is connected to the sun gear as input. Planetary gears amplify the motor torque to the outer shaft connected to the thigh brace of the exoskeleton.

ϕ_m can be expressed as

$$\phi_m = -\phi_p \cos(\omega_e t) \tag{2}$$

where ϕ_p is the peak value of permanent magnet flux linkage and the permanent magnet flux per coil satisfies

$$\phi_p \propto k_{wv} B_m r_g l_a \tag{3}$$

where k_{wv}, B_m, l_a, and r_g are winding factor, magnet working flux density, stack length, and airgap radius, respectively. The back electromotive force e can be calculated as

$$e = \frac{d\Psi_m}{dt} = N_p \frac{d\phi_m}{dt} = N_p \phi_p \omega_e \sin(\omega_e t) \tag{4}$$

where Ψ_m denotes the flux linkage in each phase winding, and N_p is the number of turns in each phase. The electrical rotating speed ω_e of the motor is

$$\omega_e = p_r \omega_m \tag{5}$$

where p_r refers to the number of rotor pole pairs and ω_m is the mechanical rotating speed. The phase current I_m can be calculated from the coil area A_c and the current density J_c as

$$I_m = A_c J_c. \tag{6}$$

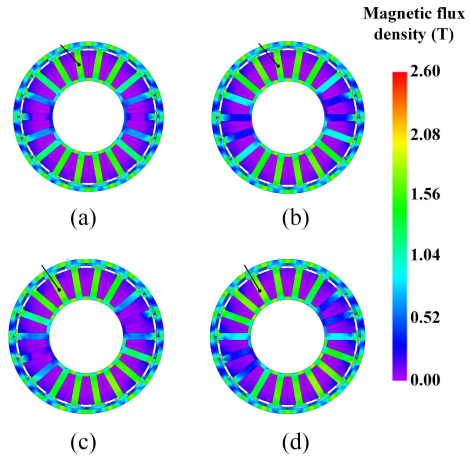

Fig. 5. Finite element method (FEM) simulation indicated that our actuator could be functional under all four conditions, including no load, nominal 6 N · m, twice overload 12 N · m, and peak 18 N · m conditions with low iron loss and high efficiency. Meanwhile, our actuator maximizes core utilization through balance between saturation effect and high output torque. (a) No load flux density. (b) Nominal 6 N · m flux density. (c) Twice overload 12 N · m flux density. (d) Peak 18 N · m flux density.

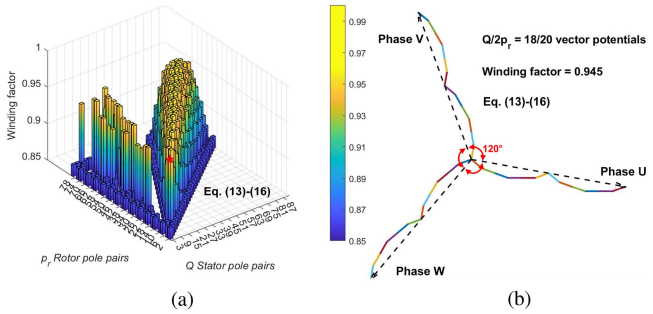

Fig. 6. (a) Our 18 stator teeth and 20 rotor pole ranked highest winding factor among various slot pole pair combinations. (Slot pole pair combinations with winding factor k_w>0.85 are shown here.) (b) Star of slot diagram of our high torque density motor benefiting from high winding factor, i.e., k_w=0.945. The three-phase phasors are symmetrically distributed to generate smooth rotating magnetic field and torque production.

Meanwhile, the winding turns in each phase are calculated as

$$N_p = k_{sf} A_s / A_c \tag{7}$$

where k_{sf} denotes the slot fill factor and A_s is the slot area. The output power can be calculated as

$$P_{\text{out}} = \eta P_{in} = \eta m N_p p_r \omega_r \phi_p I_m / 2 \tag{8}$$

where η is the efficiency. Thus, the electromagnetic torque T_e can be calculated as

$$T_e = \frac{P_{\text{out}}}{\omega_r} = \eta m p_r \phi_p k_{sf} A_s J_c / 2. \tag{9}$$

From (8) and (9), it is found that the output torque within a fixed active volume, i.e., the active torque density, is influenced by the number of phases, slot filling factor, slot area, current density, and the stator and rotor pole pairs number. A finite element method (FEM) simulation was conducted to validate the motors functionality under no load, nominal load, twice overload, and peak load conditions which can be seen in Fig. 5. It should be noted that the actual torque density is also affected by the axial length of the stator end winding.

B. Design of Armature End Winding Length of Fractional Slot Concentrated Winding for Small Thickness and Small Diameter Motors

Our motor topology employs fractional slot concentrated winding, offering the following three key advantages:

1) Low Cogging and Low Back Drive Torque: Compared to distributed winding in off-the-shelf high speed motors, fractional-slot concentrated winding eliminates the periodicity between stator teeth and rotor poles [25]. As a result, fractional-slot concentrated winding exhibits low cogging torque, which is the primary contributor to backdrive torque.

2) Short End Winding Length: The end winding length of the electric motor is closely associated with the actual torque density. It is generally influenced by

$$l_{\text{end}} = \begin{cases} k_d \cdot \frac{1}{p_r}, & \text{Distributed winding} \\ k_c \cdot \frac{1}{Q}, & \text{Fractional slot concentrated winding} \end{cases} \tag{10}$$

where Q is the number of stator teeth. The associated constants, determined empirically as in (10), satisfy the condition $k_d > k_c$. Consequently, fractional-slot concentrated winding demonstrates a shorter end winding length. The phase resistance r_{ph} can then be calculated as

$$r_{\text{ph}} = \frac{\rho l_w N_p}{a_1 A_c} \tag{11}$$

where $l_w = 2l_s + l_{\text{end}}$ is the winding length, ρ is the copper resistivity, and a_1 is the number of parallel branches.

For a motor with fractional-slot concentrated winding, the reduced end winding length decreases both the copper mass and stator winding resistance, thereby offsetting the increased copper mass resulting from a higher slot filling factor. In addition, the short-span regular coils have a reduced axial length. Consequently, for the same frame size, the motor stack length can be increased, further enhancing the torque density per unit of total volume of the motor.

3) Low Joule Losses and High Thermal Dissipation: For the electric motor with n_c coils per phase, the copper loss can be calculated as

$$P_{Cu} = m n_c I_m^2 N_p^2 \left(\frac{\rho l_w}{A_s k_{sf}} \right). \tag{12}$$

The copper loss is a function of the slot filling factor k_{sf} and winding length l_w, i.e., $P_{Cu} \propto \frac{l_w}{k_{sf}}$. With a coil span of only one tooth, tight, and neatly wound coils can be achieved.

An increased slot-filling factor effectively reduces winding copper loss for low-speed and high-torque quasi-direct-drive motors, where copper loss constitutes the dominant portion of the total loss. This makes fractional-slot concentrated winding particularly advantageous for the design of high-torque-density motors with low copper loss and high efficiency.

C. Design of Stator Teeth and Rotor Pole Pairs for High Output Torque

High-performance electric motors are required for exoskeletons, including high torque density, low back drive torque, etc. These requirements are significantly influenced by the combination of the number of stator teeth and rotor poles [26]. The selection of the most suitable stator teeth/rotor pole number combination $Q/2p_r$ is based on the evaluation of the following indices.

1) High winding factor (of main working harmonic) k_{w1} in order to enhance the torque density (13)–(16).
2) Large least common multiple between (Q, $2p_r$), in order to reduce the cogging torque (17).
3) Large and even great common divisor between (Q, $2p_r$) in order to reduce the unbalanced magnetic radial forces and increase the radial symmetry.
4) For the BLDC motor, the number of stator teeth should be multiple of the phase number.

The pitch factor is used to account for the short coil pitch configuration, which is calculated as

$$k_{\text{pv}} = \left|\sin\left(v \cdot \gamma/2\right)\right| \tag{13}$$

where v represents the spatial order of the armature field harmonic component and γ is the mechanical coil span/pitch angle, which is calculated by

$$\gamma = \frac{2\pi}{Q} \cdot \left[\frac{Q}{2p_s}\right] \tag{14}$$

where $[Q/2p_s]$ is the largest integer that not exceeds $Q/2p_s$.

The distribution factor accounting for the nonuniform distribution of windings in the stator slot is calculated as

$$k_{\text{dv}} = \frac{\left|\sin\left(\frac{qv\theta_s}{2}\right)\right|}{q\left|\sin\left(\frac{v\theta_s}{2}\right)\right|} \tag{15}$$

where θ_s is the mechanical slot pitch angle, i.e., $\frac{2\pi}{Q}$, q is the number of coil groups calculated as

$$q = Q/\left(2m \cdot t_c \cdot k_2\right) \tag{16}$$

where t_c represents motor periodicity, which is the great common divisor of (Q, p_r). k_2=1 for double layer winding while k_2=2 for single layer winding. The winding factor consists of pitch factor and distribution factor, namely $k_{\text{wv}} = k_{\text{pv}} \cdot k_{\text{dv}}$. The magnitude of cogging torque is influenced by

$$T_{\text{cog}} \propto 1/\text{LCM}\left(Q, 2p_r\right) \tag{17}$$

where LCM is the least common multiple.

According to (13)–(16), an acceptable winding factor k_{w1} (fundamental harmonic of winding factor) above 0.866 can be obtained only if the slots-per-pole-per-phase is between 1/4 and 1/2, which is defined as

$$S_{\text{pp}} = Q/\left(2p_r \cdot m\right). \tag{18}$$

If $S_{\text{pp}} < 1/4$ or $S_{\text{pp}} > 1/2$, a large portion of the rotor pole of opposite polarity is under the same stator teeth, resulting in a suppressed total back electromotive force in that phase penalizing their attainable torque density. Indicated by (8) and (9), a large rotor pole number is beneficial to high torque density as they permit thin back iron and short end windings, helping to maximize the active volume and enhance the package factor. Furthermore, the cogging torque decreases when the least common multiple between the number of stator teeth and the number of rotor poles is increased according to (17). The typical stator teeth and rotor pole pair combinations are summarized comparatively in Table III and Fig. 6(a). The optimal stator teeth and rotor pole pair number are determined to maximize the winding factor k_{wv}, electromagetic torque T_e and minimize the cogging torque T_{cog}. Based on (3), (9) and (13)–(16), the final design of 18 stator teeth and 20 rotor poles are determined, which achieves a high winding factor of 0.945. The star of slot diagram of our final design is shown in Fig. 6(b). The detailed design parameters are summarized in Table IV. Note although combinations such as 15-stator-teeth-14-rotor-pole exhibit higher winding factor, they violate index 3) and suffer from unbalanced magnetic force.

D. Planetary Gear With Low Transmission Ratio

A planetary gear mechanism seamlessly integrates the transmission with our high-torque-density motor within a limited space. Our transmission uses the sun gear ($z_s = 9$ teeth) as the input, the planetary carrier ($z_p = 34$ teeth) as the output, and the ring gear ($z_r = 78$ teeth) is fixed within the inner stator bore of the motor featuring high packaging factor. According to Willis equation, our planetary gear has a gear ratio of 9.67:1 ($n{=}z_r/z_s + 1$). Taking transmission into consideration, the torque of the actuator output shaft T_o is calculated as

$$T_o = n \cdot T_e. \tag{19}$$

IV. Mechanism Design of Foldable Hip Exoskeleton

State-of-the-art hip exoskeletons are often characterized by rigid frames and bulky structures. Although the rigid frame effectively transmits the force from the actuator to the user, it results in increased size and weight. In addition, exoskeletons with rigid frames typically require expert assistance for proper donning. Consequently, designing an exoskeleton that effectively transmits torque while remaining compact, lightweight, and capable of self-aligning to the wearer's body type, namely ensuring transparency, remains a significant challenge. Foldable mechanism designs are considered in our hip exoskeleton design. The foldable waist belt design allows the exoskeleton to better align with the wearer while the foldable thigh brace allows the exoskeleton to be mechanically transparent without any hindrance to human daily activities.

A. Foldable Waist Belt With Self-Alignment Mechanism

A foldable waist belt with a self-aligning mechanism was designed to ensure body conformity and prevent misalignment during operation. The force-free body diagram and transmission are shown in Fig. 8. Compared to our previous design, our new exoskeleton is 29% lighter and 55% smaller while being able to be made into multiple sizes to accommodate more body types. Wearable straps minimize actuator-induced motion by counteracting frame movement, namely, pulling the frame clockwise during flexion and counterclockwise during extension. The flexible frame enhances conformity, stability, and foldability

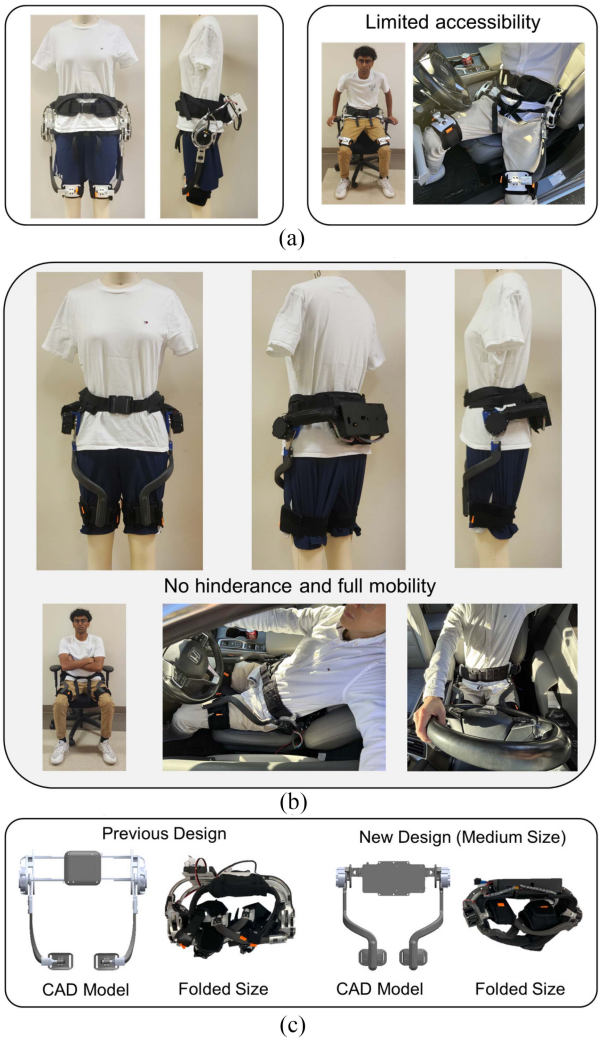

Fig. 7. Our previous exoskeleton [14] still suffers from mechanical interferences when sitting in a chair or a car seat. Benefitting from our high torque density actuator and foldable mechanism design, this exoskeleton is highly compact and unobtrusive. The previous exoskeleton used an adjustable rigid frame and was a one-size-fits-all solution with a weight of 3.7 kg and volume of 525 mm× 350 mm× 220 mm. The new robot offers small, medium, and large sizes. The medium size exoskeleton (this design) has a weight of 2.7 kg and volume of 460 mm× 180 mm× 220 mm and is more compact (55% reduction) and lightweight (29% reduction) compared to our previous design. (a) Previous hip exoskeleton with bulky size (3.7 kg). (b) This work: compact foldable portable hip exoskeleton (2.7 kg). (c) Side by side comparison of previous and current exoskeleton.

for convenient storage, accommodating various body types and enabling single-person operation. The main structure was 3D-printed using carbon fiber-infused nylon (ONYX, Markforged), balancing simplified manufacturing with high strength and stiffness through an optimized reinforcement printing method.

B. Foldable Thigh Brace With Self-Adjusting Linear Slider Mechanism

Most hip exoskeletons use a pivoting passive joint at the thigh interface, allowing the brace to tilt with the thigh angle, but additional motion occurs during hip flexion. As the

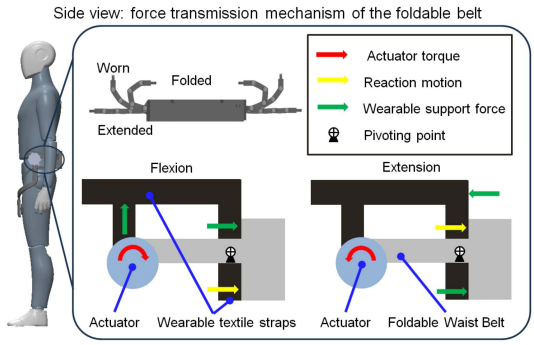

Fig. 8. Force free-body diagram of our exoskeleton to inform custom textile strap design. Our exoskeleton provides assistance for both hip flexion and extension. To minimize the induced motion about the pivoting point, we designed textile straps that are arranged to minimize wobbling of waist belt due to the reaction forces generated by the actuators.

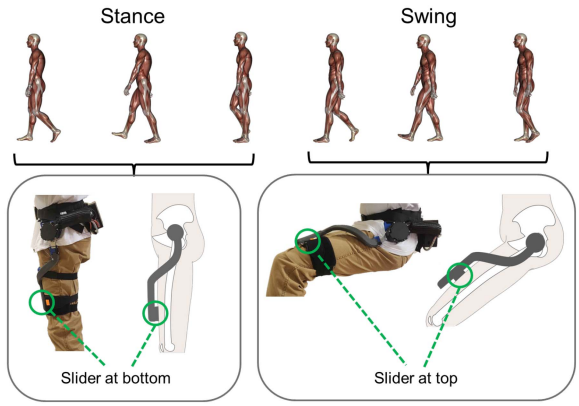

Fig. 9. Operation of the self-aligning thigh brace with a linear slider during the gait cycle. The passive self-aligning thigh brace can move linearly in parallel with the thigh axis using a roller bearing. This design was based on human biomechanics due to the fact that as the hip joint flexes, the distance from the point of rotation and the position securing the thigh arm also shortens. With the self-aligning mechanism, during the swing phase of human gait, the thigh brace can move accordingly with the wearer to prevent misalignment.

hip joint flexes, the distance between the thigh brace and the center of the actuator also shortens, as can be seen in Fig. 9. Thus, the conventional exoskeleton will press into the wearer as both ends of the thigh bar remain fixed. This fixed setup can cause discomfort, and if the hip exoskeleton fits loosely, the actuator may shift out of place during use. To solve this problem, our exoskeleton uses a sliding mechanism to provide flexing and extending assistance while allowing the thigh to move naturally. The curved thigh arm directs the actuator's force perpendicular to the thigh surface at the point where the brace wraps around it. Enabling more natural movement makes the exoskeleton feel more transparent, enhancing comfort while reducing the need for precise positioning or skill to wear it.

V. Experiments

To verify our design, we conducted benchtop and human experiments. Our actuator was connected to the hysteresis brake (PB-A-5) through the torque sensor (DYN-210) shown

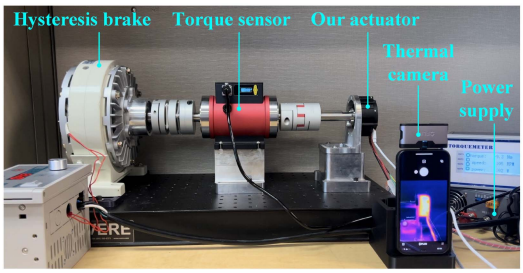

Fig. 10. Testbed setup for benchtop experiments of our actuator. The thermistor is embedded adjacent to the armature winding and power switch.

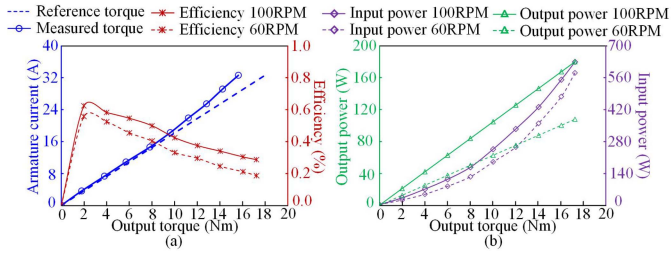

Fig. 11. Our actuator demonstrates high output torque, high output power, and high operation efficiency. (a) Predicted torque and measured torque under various armature currents; efficiency under various torque outputs. (b) Input power and output power under various torque outputs.

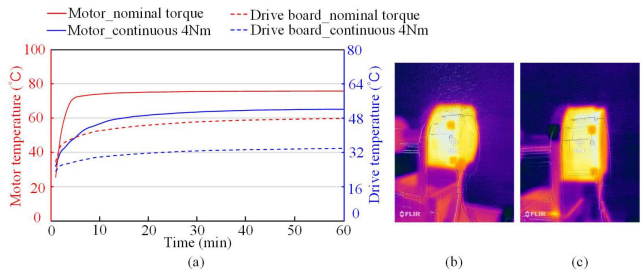

Fig. 12. Our actuator demonstrated stable thermal performance under natural air cooling. (a) Temperature under continuous nominal torque (6 N · m, red lines) is equivalent to that under assistive peak torque (18 N · m) according to the integral equivalence principle. Another light-load working condition (4 N · m, blue lines) is also exhibited. (b) and (c) Steady-state temperature after one hour of continuous nominal torque and continuous 4 N · m torque, respectively.

in Fig. 10. All subjects were informed of the experiment protocol and consented before participating in the experiments. Our protocol was approved by Institutional Review Board at NCSU No. eIRB #26017.

A. High Torque Density Actuator for Compact Exoskeleton

To validate the actual performances of our actuator, we built the benchtop and conducted comprehensive experiments as indicated in Figs. 11 and 12. It was tested across various torque outputs at a shaft speed of 100 r/min to fully meet the biological joint speed requirements. The measured torque matches well with the predicted torque as shown in Fig. 11(a). The deviation of torque becomes relatively larger as the current goes up due to the saturation effect. Moreover, the input power, output power, and efficiency were measured under 60 r/min and 100 r/min, respectively. The measured results demonstrated high output torque, high output power, and high operation efficiency, as shown in Fig. 11(a) and (b). In addition, the temperature variations of the motor hot spot, namely armature winding, and the motor drive are measured under nominal load and continuous 4 N · m load. The measured results indicated stable thermal performance in natural air cooling. Furthermore, the performance of our actuator compared with off-the-shelf high-speed motor and quasi-direct-drive actuators was summarized in Table V, including conventional high-speed motor Maxon EC45, quasi-direct-drive MyActuator RMD-X8 and quasi-direct-drive T-motor AK80-9. Among these, our actuator delivered the highest torque density in the pool. Furthermore, our actuator achieved the highest package factor with the lowest weight and the smallest size among all quasi-direct-drive actuators. This is critical for low backdrive torque and natural movements [27]. As shown in Fig. 7, the proposed hip exoskeleton weighs 2.7 kg, a significant reduction compared to our previous hip exoskeleton, 3.7 kg in [14]. This is attributed to the high torque density of our actuator and the foldable mechanism design, making the new exoskeleton compact, portable, and unobtrusive in daily living.

B. Metabolic Cost Reduction During Walking With Young and Older Adults

To meet the multifaceted requirements of exoskeletons, we not only evaluated their mechatronic performance, but also assessed their human assistance performance, specifically focusing on net metabolic cost reduction which is between Assist On versus No Exo. Measured metabolic cost refers to energy expenditure during a task after subtracting the resting metabolic rate. Note gross metabolic reduction is between assist on versus assist off. We recruited nine non-disabled subjects (6 young: 4 males, 2 females, age 29.2 $\pm$ 4.66; 3 older: 2 male, 1 female, age 68.67 $\pm$ 1.7) and measured their metabolic rate using an analyzer mask (volume of oxygen consumed (VO2) Master). We began with walking tests, as it is one of the most common daily activities. The treadmill walking trials were conducted with the eight non-disabled participants under two conditions, with assistance from our exoskeleton and without our exoskeleton. Each subject walked on the treadmill at a speed of 1.25 m/s for six minutes under one condition, following a test period of 10 min. Afterward, the subject walked at the same speed for another six minutes under another condition. The last two-minute net metabolic results were analyzed as shown in Fig. 13(a). The net metabolic rate was reduced by 13.75% on average for 1.25 m/s walking with our exoskeleton assistance compared to the No Exo condition for young adults, which is a larger reduction than the state-of-the-art hip exoskeleton reported in [8] with a reduction of 9.3% for 1.5 m/s walking and thus validating our actuator and mechanical design. Our robot can assist both extension and flexion for the hip joint while the robot in [8] can only assist extension. The objective of human subject experiments was to demonstrate the mechatronics capability, but not to minimize metabolic cost rate. Thus, we used Samsung's controller [28] to benchmark with the state-of-the-art instead of

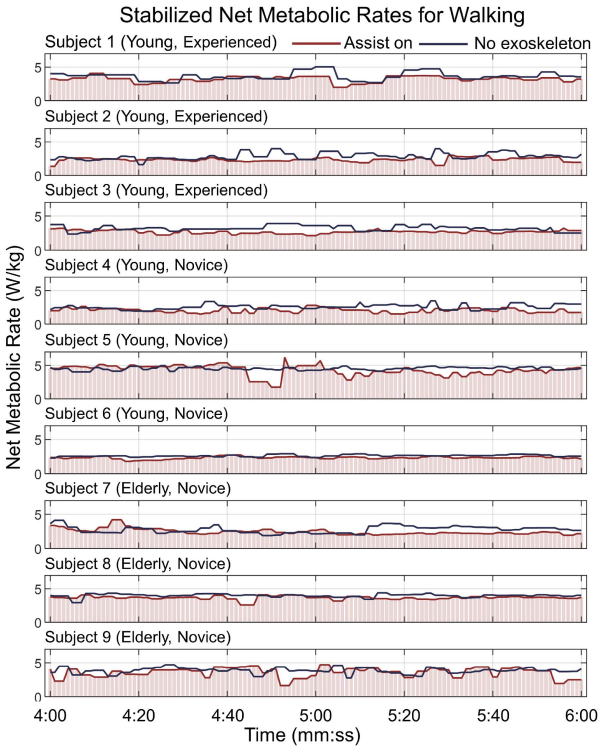

Fig. 13. Our exoskeleton helped reduce net metabolic cost for both walking and stair climbing as well as for both young and older adults. There are 3 novice exoskeleton users in the 6 young adults and all 3 older subjects are novice users. (a) Walking test of young ($n = 6$) and older ($n = 3$) subjects. (b) Stair climbing test of young subjects ($n = 6$).

our RL controller. Furthermore, the maximum assistive torque was individually tuned based on each user's preference. For all participants, the peak assistive torque was within the range of 6–8 Nm. Experienced users typically exhibited larger metabolic cost reduction [29]. In this article, 3 out of 6 young adults were novice users, so if all the subjects were experienced users, the overall net metabolic reduction may reduce further.

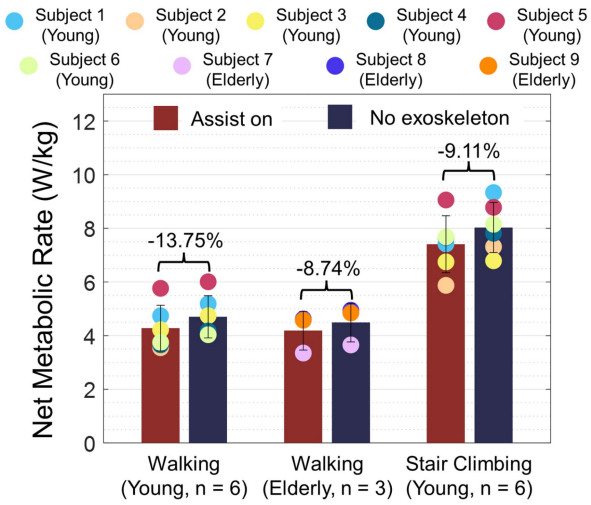

Fig. 14. Net metabolic rate results for walking and stair climbing experiments for all populations. The average net metabolic rate was reduced by 13.75% for young adults and reduced by 8.74% for older adults during walking at 1.25 m/s. It was reduced by 9.11% for young adults during stair climbing.

C. Metabolic Cost Reduction During Stair Climbing With Young Adults

Stair climbing is another common activity for assistance in daily living. The experiment was conducted using a StairMaster stair machine at level 7 (60 steps/minute), involving six non-disabled young subjects. Each subject climbed the stairs for six minutes with and without the exoskeleton. A 10-min break between each trial is arranged. The net metabolic cost during the stair climbing experiment decreased by 9.11% on average as shown in Fig. 13(b). These results (see Fig. 14) demonstrated that our robot can reduce metabolic cost during walking and stair climbing with both flexion and extension assistance of hip joints.

VI. Conclusion

Our actuator and two foldable mechanism were designed heuristically, which may not provide the optimal solution for maximizing overall performance. To isolate the impact of control algorithms, we employed the same gait cycle-based controller [28] in our robot to evaluate metabolic cost reduction, aiming to understand the contribution of the mechatronic design. Preliminary results from human subject experiments demonstrated the feasibility of our exoskeleton in reducing metabolic cost for both young and older adults, likely due to our lightweight design minimizing metabolic cost penalties. In this article, we focus on studying the assistive effects (immediate effect) of mobility support for non-disabled young and older adults. Our long-term vision is to assist both non-disabled individuals and those with gait impairments, including musculoskeletal conditions such as sarcopenia (muscle weakness) and hip osteoarthritis, as well as neurological impairments like Parkinson's disease. One limitation of the 3D-printed waist belt is its softness, which may compromise the efficiency of delivering

more than 10 Nm torque. Future work will involve metal material design of waist belt and systematic human experiments to understand capability of our robot.

Acknowledgment

Any opinions, findings, and conclusions, or recommendations expressed in this material are those of the authors and do not necessarily reflect the views of the funding organizations.

References

[1] J. Kim et al., "Soft robotic apparel to avert freezing of gait in Parkinson's disease," *Nature Med.*, vol. 30, no. 1, pp. 177–185, 2024.
[2] Z. F. Lerner, D. L. Damiano, and T. C. Bulea, "A lower-extremity exoskeleton improves knee extension in children with crouch gait from cerebral palsy," *Sci. Transl. Med.*, vol. 9, no. 404, 2017, Art. no. eaam9145.
[3] T.-H. Huang et al., "Modeling and stiffness-based continuous torque control of lightweight quasi-direct-drive knee exoskeletons for versatile walking assistance," *IEEE Trans. Robot.*, vol. 38, no. 3, pp. 1442–1459, Jun. 2022.
[4] S. Luo et al., "Experiment-free exoskeleton assistance via learning in simulation," *Nature*, vol. 630, no. 8016, pp. 353–359, 2024.
[5] P. Slade, M. J. Kochenderfer, S. L. Delp, and S. H. Collins, "Personalizing exoskeleton assistance while walking in the real world," *Nature*, vol. 610, no. 7931, pp. 277–282, 2022.
[6] N. V. Divekar, G. C. Thomas, A. R. Yerva, H. B. Frame, and R. D. Gregg, "A versatile knee exoskeleton mitigates quadriceps fatigue in lifting, lowering, and carrying tasks," *Sci. Robot.*, vol. 9, no. 94 2024, Art. no. eadr8282.
[7] B. Lim, J. Jang, J. Lee, B. Choi, Y. Lee, and Y. Shim, "Delayed output feedback control for gait assistance and resistance using a robotic exoskeleton," *IEEE Robot. Autom. Lett.*, vol. 4, no. 4, pp. 3521–3528, Oct. 2019.
[8] J. Kim et al., "Reducing the metabolic rate of walking and running with a versatile, portable exosuit," *Science*, vol. 365, no. 6454, pp. 668–672, 2019.
[9] C. Buesing et al., "Effects of a wearable exoskeleton stride management assist system (SMA) on spatiotemporal gait characteristics in individuals after stroke: A randomized controlled trial," *J. Neuroengineering Rehabil.*, vol. 12, pp. 1–14, 2015.
[10] S. W. John, K. Murakami, M. Komatsu, and S. Adachi, "Cross-wire assist suit concept, for mobile and lightweight multiple degree of freedom hip assistance," in *Proc. Int. Conf. Rehabil. Robot.*, 2017, pp. 387–393.
[11] F. Giovacchini et al., "A light-weight active orthosis for hip movement assistance," *Robot. Auton. Syst.*, vol. 73, pp. 123–134, 2015.
[12] T. G. Sugar, E. Fernandez, D. Kinney, K. W. Hollander, and S. Redkar, "Hesa, hip exoskeleton for superior assistance," in *Proc. Wearable Robot.: Challenges Trends: Proc. 2nd Int. Symp. Wearable Robot.*, 2017, pp. 319–323.
[13] I. Kang, H. Hsu, and A. J. Young, "Design and validation of a torque controllable hip exoskeleton for walking assistance," in *Dynamic Syst. Control Conf.*, vol. 51890. American Society of Mechanical Engineers, 2018, pp. 1–13.
[14] D. Rodríguez-Jorge et al., "Biomechanics-informed mechatronics design of comfort-centered portable hip exoskeleton: Actuator, wearable interface, controller," *IEEE Trans. Med. Robot. Bionics*, vol. 7, no. 2, pp. 687–698, May 2025.
[15] S. Yu et al., "Quasi-direct drive actuation for a lightweight hip exoskeleton with high backdrivability and high bandwidth," *IEEE/ASME Trans. Mechatron.*, vol. 25, no. 4, pp. 1794–1802, Aug. 2020.
[16] A. Tenconi, S. Vaschetto, and A. Vigliani, "Electrical machines for high-speed applications: Design considerations and tradeoffs," *IEEE Trans. Ind. Electron.*, vol. 61, no. 6, pp. 3022–3029, Jun. 2014.
[17] J. Lin, N. V. Divekar, G. C. Thomas, and R. D. Gregg, "Optimally biomimetic passivity-based control of a lower-limb exoskeleton over the primary activities of daily life," *IEEE Open J. Control Syst.*, vol. 1, pp. 15–28, 2022.
[18] J. K. Leestma, S. Mathur, M. D. Anderton, G. S. Sawicki, and A. J. Young, "Dynamic duo: Design and validation of an autonomous frontal and sagittal actuating hip exoskeleton for balance modulation during perturbed locomotion," *IEEE Robot. Autom. Lett.*, vol. 9, no. 5, pp. 3995–4002, May 2024.
[19] X. Xing, S. Zhang, T. Huang, J. S. Huang, H. Su, and Y. Li, "Spatial iterative learning torque control of robotic exoskeletons for high accuracy and rapid convergence assistance," *IEEE/ASME Trans. Mechatron.*, vol. 29, no. 6, pp. 4215–4227, May 2024.
[20] S. Yu et al., "Design and control of a high-torque and highly backdrivable hybrid soft exoskeleton for knee injury prevention during squatting," *IEEE Robot. Autom. Lett.*, vol. 4, no. 4, pp. 4579–4586, Oct. 2019.
[21] S. V. Sarkisian, M. K. Ishmael, and T. Lenzi, "Self-aligning mechanism improves comfort and performance with a powered knee exoskeleton," *IEEE Trans. Neural Syst. Rehabil. Eng.*, vol. 29, pp. 629–640, 2021.
[22] Y. Lee et al., "Biomechanical design of a novel flexible exoskeleton for lower extremities," *IEEE/ASME Trans. Mechatron.*, vol. 22, no. 5, pp. 2058–2069, Oct. 2017.
[23] A. Bajpai et al., "Design and validation of a versatile high torque quasidirect drive hip exoskeleton," *IEEE/ASME Trans. Mechatron.*, vol. 29, no. 1, pp. 789–797, Feb. 2024.
[24] G. Lei, C. Liu, J. Zhu, and Y. Guo, "Techniques for multilevel design optimization of permanent magnet motors," *IEEE Trans. Energy Convers.*, vol. 30, no. 4, pp. 1574–1584, Dec. 2015.
[25] E. Fornasiero, L. Alberti, N. Bianchi, and S. Bolognani, "Considerations on selecting fractional-slot nonoverlapped coil windings," *IEEE Trans. Ind. Appl.*, vol. 49, no. 3, pp. 1316–1324, May/Jun. 2013.
[26] E. Carraro, N. Bianchi, S. Zhang, and M. Koch, "Design and performance comparison of fractional slot concentrated winding spoke type synchronous motors with different slot-pole combinations," *IEEE Trans. Ind. Appl.*, vol. 54, no. 3, pp. 2276–2284, May/Jun. 2018.
[27] J. Zhu, C. Jiao, I. Dominguez, S. Yu, and H. Su, "Design and backdrivability modeling of a portable high torque robotic knee prosthesis with intrinsic compliance for agile activities," *IEEE/ASME Trans. Mechatron.*, vol. 27, no. 4, pp. 1837–1845, Aug. 2022.
[28] B. Lim et al., "Delayed output feedback control for gait assistance with a robotic hip exoskeleton," *IEEE Trans. Robot.*, vol. 35, no. 4, pp. 1055–1062, Aug. 2019.
[29] K. L. Poggensee and S. H. Collins, "How adaptation, training, and customization contribute to benefits from exoskeleton assistance," *Sci. Robot.*, vol. 6, no. 58, 2021, Art. no. eabf1078.

Yuming Yan received the B.Eng. degree in electrical engineering from Xi'an Jiaotong University (XJTU), Xi'an, China, in 2017 and the Ph.D. degree in electrical engineering from the School of Electrical and Electronic Engineering, Nanyang Technological University, Singapore, in 2024.

He was a Postdoctoral Research Fellow with the Department of Mechanical and Aerospace Engineering, North Carolina State University, Raleigh, NC, USA. He is currently a Postdoctoral Research Fellow with the Tandon School of Engineering, New York University, New York, NY, USA. His research interests include electric machines and drives, design and control of assistive and rehabilitative wearable robots.

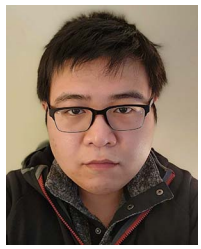

Jin Sen Huang received the Bachelor of Science degree in mechanical engineering, in 2018, and the Master of Science degree in mechanical engineering in 2023 from North Carolina State University, Raleigh, NC, USA, where he is currently working toward the Ph.D. degree in mechanical engineering.

His current research interests include mechatronics design of wearable robots.

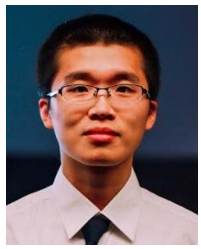

Junxi Zhu (Graduate Student Member, IEEE) received the B.S. degree from Shanghai Jiao Tong University, Shanghai, China, in 2011, the M.S. degree from the University of Maryland, College Park, College Park, MD, USA, in 2015, and the Ph.D. degree North Carolina State University, Raleigh, NC, USA, in 2024, all in mechanical engineering.

His current research interest includes mechatronics, controller design and controller implementation of the wearable robot.

Zhimin Hou received the B.E. degree in mechanical engineering from Tongji University, Shanghai, China, in 2016, the M.S. degree in mechanical engineering from Tsinghua University, Beijing, China, in 2019, and the Ph.D. degree in biomedical engineering from the National University of Singapore, Singapore, in 2024.

He was a Postdoctoral Research Fellow with the Department of Mechanical and Aerospace Engineering, North Carolina State University, Raleigh, NC, USA. He is currently a Postdoctoral Research Fellow with the Tandon School of Engineering, New York University, New York, NY, USA. His research interests include reinforcement learning, intelligent control, and physical human–robot interaction.

Weibo Gao (Graduate Student Member, IEEE) received the B.S. degree from Xi'an Jiao Tong University, Xi'an, China, in 2017 and the M.S. degree from the University of Pittsburgh, Pittsburgh, PA, USA, in 2019, both in mechanical engineering. He is currently working toward the Ph.D. degree in mechanical engineering with North Carolina State University, Raleigh, NC, USA, under the supervision of Dr. Hao Su.

His current research interest includes mechatronics design and control of wearable robots and surgical robots.

Ivan Lopez-Sanchez received the B.E. degree in aerospace engineering from Universidad Autónoma de Baja California-FCITEC, Tijuana, México, in 2016 and the M.Sc. and Pd.D. degrees in digital systems with specialization in control systems from Instituto Politécnico Nacional-CITEDI, Tijuana, México, in 2019 and 2023, respectively.

He is currently a Postdoctoral Research Fellow with the Tandon School of Engineering, New York University, New York, NY, USA. His research interests include nonlinear control, neural network-based control, wearable robotics, and unmanned aerial vehicles.

Nitin Srinivasan received the B.Tech. degree from the Dayananda Sagar College of Engineering, Bengaluru, India, and the M.S. degree from North Carolina State University, Raleigh, NC, USA, both in mechanical engineering, in 2021 and 2024, respectively.

His current research interests include the design and control of electromechanical systems, with applications in medical devices.

Advaith Srihari is currently working toward the B.S. degree in mechanical engineering with the Department of Mechanical and Aerospace Engineering, North Carolina State University, Raleigh, NC, USA.

He is currently an Undergraduate Research Assistant with the Biomechatronics and Intelligent Robots Lab, where he focuses on the design and testing of wearable robots. His academic interests include robotics and mechanical design, and he plans to pursue a graduate degree specializing in controls and automation.

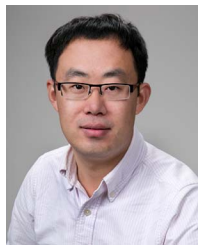

Hao Su (Senior Member, IEEE) received the B.S. degree in automation from the Harbin Institute of Technology, Harbin, China, in 2006, the M.S. degree in mechanical engineering from the State University of New York University, Buffalo, NY, USA, in 2008, and the Ph.D. degree in mechanical engineering from Worcester Polytechnic Institute, Worcester, MA, USA, in 2013.

He is currently an Associate Professor with the Tandon School of Engineering, New York University (NYU), New York, NY, USA. He was an Associate Professor with the Department of Mechanical and Aerospace Engineering, North Carolina State University, Raleigh, NC, USA, and also in the joint NCSU/UNC Biomedical Engineering Department, University of North Carolina Chapel Hill, Chapel Hill, NC, USA. He was a Research Scientist with Philips Research North America, Cambridge, MA, USA, and, then, a Postdoctoral Fellow with Harvard University, Cambridge, MA, USA, and Wyss Institute for Biologically Inspired Engineering, Boston, MA, USA.

Prof. Su is a recipient of the National Science Foundation CAREER Award and Switzer Distinguished Fellowship of the U.S. Department of Health and Human Services. He is a Technical Editor of ASME/IEEE TRANSACTION ON MECHATRONICS, and an Associate Editor for IEEE ROBOTICS AND AUTOMATION MAGAZINE, IEEE International Conference on Robotics and Automation, and IEEE/RSJ International Conference on Intelligent Robots and Systems.